Journal of Alloys and Compounds 1057 (2026) 186955

Contents lists available at ScienceDirect

Journal of Alloys and Compounds

journal homepage: www.elsevier.com/locate/jalcom

Volume energy density induced grain refinement and enhanced mechanical properties of FeCoCrNiMn high-entropy alloy fabricated by selective laser melting (SLM)

Tao He [a,1], Jiani Huang [b,1], Muhammad Rehan [a], Linhe Sun [a], Wenjie Lu [b], Juan Chen [a,c], Yinhui Wang [c], Hui Deng [c], Suet To [a], Xusheng Yang [a,*], Wai Sze Yip [a,*]

[a] State Key Laboratory of Ultra-precision Machining Technology, Department of Industrial and Systems Engineering, The Hong Kong Polytechnic University, Hung Hom, Kowloon, Hong Kong
[b] Department of Industrial and Systems Engineering, The Hong Kong Polytechnic University, Hung Hom, Kowloon, Hong Kong
[c] Department of Mechanical and Energy Engineering, Southern University of Science and Technology, Shenzhen 518055, China

ARTICLE INFO

Keywords:
High-entropy alloy
Selective laser melting
Volume energy density
Mechanical properties
Grain refinement

ABSTRACT

This study investigates the influence of volume energy density on the microstructure and mechanical properties of FeCoCrNiMn high-entropy alloy fabricated by selective laser melting (SLM). By systematically varying the laser processing parameters, the effects on crystal morphology, grain refinement, and mechanical performance, including porosity, tensile strength, microhardness, and wear resistance, were evaluated. The results demonstrate that lower volume energy density promotes significant grain refinement, increases the density of grain boundaries and twins, and leads to the formation of a checkerboard-like crystal structure. These microstructural features enhance the alloy's ability to store dislocations and energy, resulting in improved yield strength and maximum tensile strength. In contrast, higher volume energy density increases porosity, grain size, and texture strength, and induces a predominantly intragranular fracture mode, which contributes to improved uniform elongation. Overall, precise control of volume energy density during SLM processing enables the optimization of grain structure and mechanical properties, achieving a desirable balance of tensile performance, strain hardening, toughness, and wear resistance in FeCoCrNiMn high-entropy alloys.

1. Introduction

Selective laser melting (SLM) technology, as a widely adopted technique in the field of additive manufacturing, enables the direct fabrication of structurally complex components while supporting environmentally friendly design. Compared with traditional methods such as casting, vacuum induction melting, and hot press sintering, SLM enhances processing efficiency and reduces equipment costs, thereby promoting the sustainable utilization of metal powders. Through rapid melting and solidification involving multiple solid-liquid-solid phase transitions, SLM not only leverages a high temperature gradient and a rapid cooling rate to suppress the formation of detrimental secondary phases in alloys but also facilitates the growth of columnar grains and submicron cellular structures [1,2]. Numerous studies [3–5] have demonstrated that a uniform, single-phase face-centered cubic (FCC) solid solution exhibits superior properties, including high hardness, oxidation resistance, and wear resistance. An extensive formation of columnar grains alters the fracture behavior of the material, resulting in transgranular fracture as the dominant mode and significantly enhancing the metal's toughness. The presence of submicron crystalline structures effectively impedes dislocation motion and increases dislocation storage, thereby improving fracture resistance and tensile strength [6,7]. Therefore, as a promising class of multi-component metallic materials, high-entropy alloys developed using SLM technology can leverage the advantages offered by this technique.

Compared with conventional binary alloys, high-entropy alloys are typically composed of more than five metallic elements. Due to their high mixing entropy, these alloys tend to suppress the formation of complex intermetallic compounds and instead favor the development of simple crystal structures, such as FCC phases. Alloys with such structures

---

* Corresponding authors.
E-mail addresses: xusheng.yang@polyu.edu.hk (X. Yang), lenny.ws.yip@polyu.edu.hk (W.S. Yip).

[1] These authors contributed equally to this work

https://doi.org/10.1016/j.jallcom.2026.186955

often exhibit a range of desirable mechanical properties. Among them, the five-element high-entropy alloys composed of Fe, Co, Cr, Ni, and Mn have been extensively studied for their superior mechanical performance [8]. The FeCoCrNiMn alloy was initially introduced by Cantor et al. in 2004 [9]. It exhibits a typical FCC structure, where Fe, Co, and Ni act as FCC stabilizers, while Cr and Mn contribute to corrosion resistance and diversity in mechanical properties. The minute differences in atomic radius among these five elements promote the formation of stable solid solutions rather than simple intermetallic compounds, resulting in high strength, ductility, corrosion resistance, and thermal stability. FeCoCrNiMn alloys offer an exceptional strength-to-weight ratio and outstanding low-temperature toughness, making them ideal candidates for the fabrication of lightweight, high-strength structural components. This indicates significant potential for application in the aerospace field. In the medical field, their excellent biocompatibility and mechanical properties make them promising candidates for customized orthopedic implants and dental restorations, particularly in environments requiring high strength and corrosion resistance [10].

Furthermore, FeCoCrNiMn alloys fabricated via SLM technology exhibit a plasticity enhancement effect induced by nano-twinning under fatigue loading, further expanding their applicability in high-cycle fatigue environments [11]. Extensive research on this alloy has confirmed their excellent processing adaptability and microstructural stability in additive manufacturing, making them ideal model material for investigating the processing characteristics and property development of high-entropy alloys. Xu et al. [12] reported that FeCoCrNiMn alloys fabricated using the SLM technique exhibited uniform elemental distribution and a microstructure consisting of honeycomb sub grains with grain boundary angles less than 5°. Liu et al. [13] prepared FeCoCrNiMn using the SLM technique and observed a single FCC phase characterized by columnar dendrites. Additionally, the high cooling rate during the SLM process resulted in a high density of dislocations and substructures, enhancing the alloy's dynamic yield strength and strain hardening rate. Chew et al. [14] fabricated a CoCrFeNiMn alloy with high strength via laser-assisted printing, achieving a yield strength of 518 MPa and a tensile strength of 660 MPa. This enhancement was primarily attributed to grain boundary strengthening due to refined grains.

To further improve the performance of high-entropy alloys and investigate the evolution of their mechanical properties, researchers have begun to examine how laser parameters affect the microstructure and properties of these alloys. During the laser printing process of FeCoCrNiMn, the optimization of laser parameters plays a critical role, directly impacting the alloy's microstructure, mechanical performance, and overall forming quality. Some researchers have introduced the concept of volumetric energy density (VED), suggesting that in SLM processes, both the laser scanning speed and laser power jointly determine the VED, which in turn affects the melt pool temperature distribution, cooling rate, and solidification behavior. Therefore, the combined effect of these parameters on alloy properties can be evaluated by normalizing the influence of scanning speed and laser power. For instance, Li et al. [15] found that a VED of 74 J/mm^3 yielded FeCoCrNiMn specimens with a relative density of 98.2 % and significantly improved surface finish In addition, Zheng et al. [16] found that changing the scanning speed and laser power under a constant VED can result in variations in crystal structure and texture orientation, thus influencing the alloy's mechanical properties at the microstructural level. These findings offer essential guidance for optimizing SLM laser parameters, as the selection of an appropriate VED can significantly improve the mechanical performance and printing quality of the material.

Although previous studies have demonstrated that optimizing laser parameters such as scanning speed and laser power can significantly reduce printing defects and improve mechanical properties of FeCoCrNiMn high-entropy alloys produced by SLM, the application of SLM technology in the FeCoCrNiMn system remains in its exploratory phase. Due to the relatively narrow range of current laser parameters such as scanning speed and laser power exploration and the failure to comprehensively and systematically correlate printing parameters with the microstructure and mechanical properties of the material, challenges remain in studying the forming mechanism and optimizing parameters. Therefore, there is an urgent need for a systematic and comprehensive investigation into how a broader range of laser parameters influence the microstructural evolution and mechanical properties of this alloy. In this study, FeCoCrNiMn high-entropy alloys were fabricated by SLM using different laser parameters. The mechanical properties of the resulting specimens, including hardness, tensile strength, and strain hardening rate, were compared, and their microstructures were analyzed. By correlating specific laser processing conditions with observed changes in microstructure and mechanical behavior, this work provides a detailed understanding of the underlying mechanisms governing property evolution in SLM-processed high-entropy alloy. Ultimately, these findings offer valuable insights into the targeted optimization of laser parameters, contributing to the development of high-performance high-entropy alloys with tailored properties.

2. Experimental procedure

2.1. Powders and sample preparation

FeCoCrNiMn high-entropy alloy powders with equiatomic composition were prepared using the vacuum induction melting gas atomization method. The equipment employed was a VIGA-100 vacuum induction melting gas atomization system, which consists of two main components: a vacuum induction melting furnace and a powder production system. To produce the equiatomic FeCoCrNiMn powder, ingots of five different elements—Fe, Co, Cr, Ni, and Mn—were placed into the melting furnace and subjected to high-temperature melting at 1500°C for a holding time of 40 min. After thorough alloying, the molten alloy was directed into the powder production system located beneath the furnace. It was discharged through a nozzle beneath the insulated crucible and atomized into fine droplets by high-pressure argon gas. These droplets gradually solidify into spherical powder particles. Subsequently, the oxygen content of the powders was analyzed using an oxygen-nitrogen analyzer, and X-ray diffraction (XRD) analysis was performed, as shown in Fig. 1. Fig. 1a presents the oxygen content results based on two independent measurements. The average oxygen content in the powder was only 0.027318 %, indicating that no oxidation occurred during the preparation of the FeCoCrNiMn powder through atomization. The XRD results shown in Fig. 1b confirm that no secondary phases were present in the atomization-derived FeCoCrNiMn powder.

The particle size distribution and chemical composition are presented in Figs. 2b and 2c. The five elements in the high-entropy alloy are distributed relatively evenly. The particle size of the powder is mostly below 40 μm, with an average particle size of 14.38 μm. Finer powders were more readily melted, facilitating improved densification of the specimens. These high-entropy alloy powders were loaded into a SLM system and processed under a vacuum and argon atmosphere, as illustrated in Fig. 2a. A layer-by-layer printing strategy was employed to fabricate nine rectangular specimens, each measuring 20 mm in length, 13 mm in width, and 3 mm in height. To minimize thermal stresses between layers in the building direction, the laser scanning direction was rotated by 67° between each layer, with a scanning pitch of 0.06 mm and a layer thickness of 0.03 mm, as shown in Figs. 2d and 2e. The nine specimens were fabricated using different laser parameters, including variations in laser power and scanning speed. Specifically, the laser power ranged from 200 W to 440 W, and the scanning speed varied from 400 mm/s to 1200 mm/s, as detailed in Table 1. A laser power range of 200–400 W promoted the formation of a uniform FCC single-phase structure, resulting in excellent mechanical properties and density. Printing speeds between 400 and 1200 mm/s were better suited to different laser powers, enabling investigation into the causes of

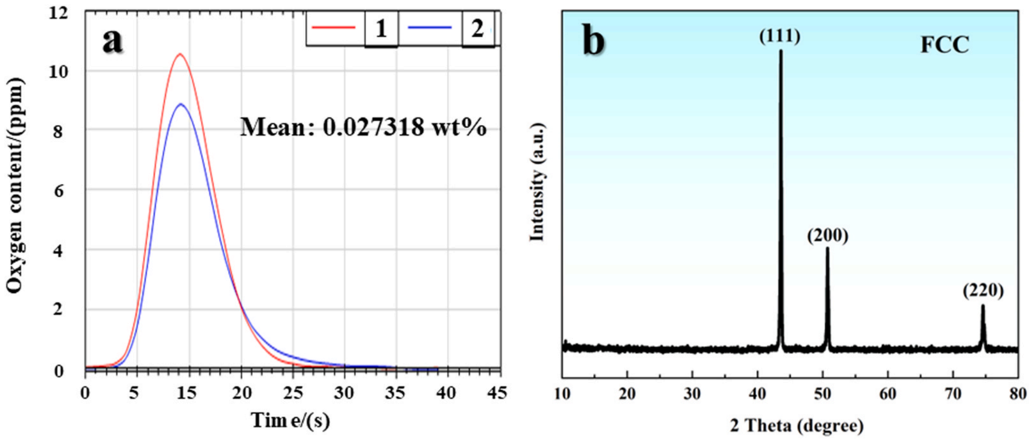

Fig. 1. (a) Oxygen content and (b) XRD results of FeCoCrNiMn powder.

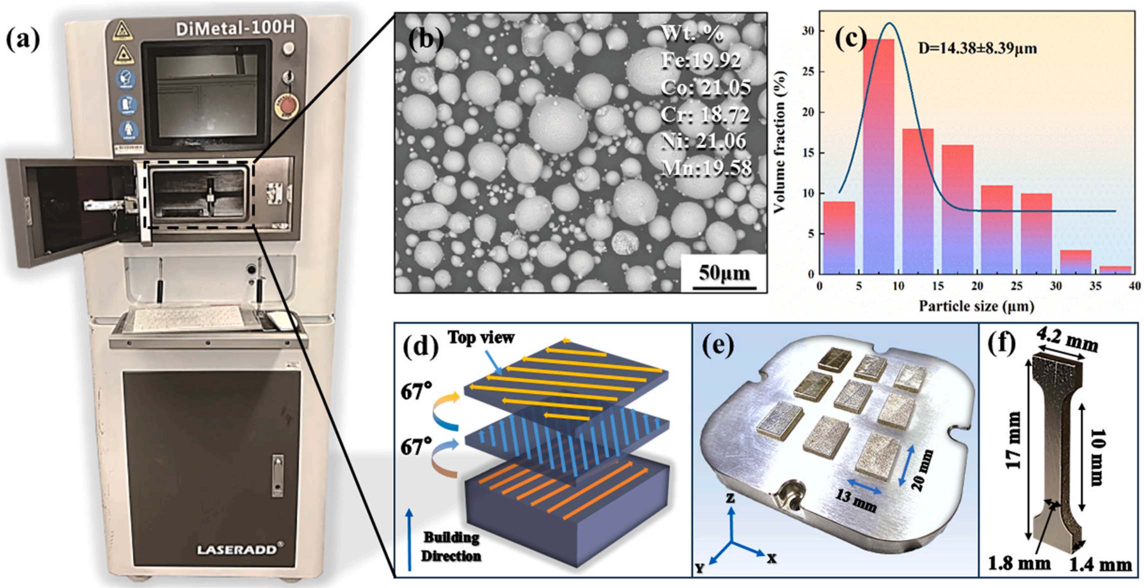

Fig. 2. (a) Printing machine of SLM; (b) Powder morphology of FeCoCrNiMn; (c) Particle size distribution; (d) SLM forming principle; (e) Printed samples of FeCoCrNiMn; (f) Sample size dimension for tensile test.

Table 1
SLM process parameters of FeCoCrNiMn sample.

High-entropy alloy	Laser power (W)	Scanning velocity (mm/s)	Hatching space (mm)	Layer thickness (mm)	VED (J/mm^3)
FeCoCrNiMn	200	1200	0.06	0.03	92.59
	200	800			138.89
	200	400			277.78
	320	1200			148.15
	320	800			222.22
	320	400			444.44
	440	1200			203.70
	440	800			305.56
	440	400			611.11

overheating cracks and porosity, as well as the growth behavior of coarse and fine grains [17]. This approach further contributes to the optimization of printing parameters for enhanced printing outcomes.

The VED (E) used in this study is defined as follows [18]:

$$E = \frac{P}{V \bullet H \bullet L} \tag{1-1}$$

where P represents the laser power (W), V is the scanning velocity (mm/s), H is the hatching space(mm), and L is the layer thickness (mm).

2.2. *Microstructure characterization*

The FeCoCrNiMn specimens printed on a 316 L stainless steel substrate were sequentially sectioned using a wire cutter. The surfaces were polished with 400, 800, 1200, 1500, and 2000 mesh sandpapers by an automatic grinding and polishing machine. Following initial microstructural observation using a scanning electron microscope (Hitachi TM3000), the specimens were electrolytically polished in a perchloric acid electrolyte solution with a voltage of 20 V, an electrolysis time of 10 s, and an ethanol-to-perchloric acid volume ratio of 9:1. Subsequently, the microstructures and crystallographic information were examined using a scanning electron microscope (Thermo Scientific Apreo 2) equipped with energy-dispersive spectroscopy (EDS) and electron backscatter diffraction (EBSD) detectors. A high-precision optical profiler (Zygo) was employed to analyze the specimen surfaces after the wear test.

2.3. *Mechanical tests*

To comprehensively evaluate the mechanical properties of the specimens, microhardness, tensile strength, and wear resistance were assessed. For microhardness testing, a Struers Duramin-40 microhardness tester was used to measure the surface-polished specimens. Five measurements were taken at different positions under a controlled load of 200 g with a dwell time of 10 s. Tensile properties were evaluated using a Zwick Roell Z020 TEW universal testing machine equipped with a laser extensometer. Flat dog-bone-shaped tensile specimens with dimensions of 1 mm × 2 mm × 4 mm (thickness × width × length) were fabricated via wire cutting, with the tensile direction oriented perpendicular to the building direction, as shown in Fig. 2 f. For dry wear testing, an Anton Paar tribometer was employed. Prior to testing, the specimen surfaces were polished, and the wear tests were conducted using aluminum oxide grinding balls under a load of 5 N for 20 min for each sample.

3. Results and discussion

3.1. *Microstructure and grain morphology*

3.1.1. *Porosity*

Fig. 3 illustrates the porosity of the printed samples under various laser parameters. The results indicate that increasing the laser power while decreasing the scanning speed leads to a greater number of voids on the sample surface. This trend is further clarified by examining the VED values listed in Table II. Notably, the highest pore density is observed at a 611.11 J/mm^3 , as shown in Fig. 3 g. In contrast, when the VED is below 277.78 J/mm^3 , the samples display fewer surface pores, improved surface finish, and higher overall density, as illustrated in Figs. 3b, 3c, 3e, 3 f, and 3i. These observations suggest that there is an optimal range of VED for minimizing porosity and enhancing the quality of SLM-fabricated high-entropy alloys. Applying a VED that is too high can result in excessive pore formation, while a lower, more controlled VED promotes better densification and surface quality. This finding is consistent with previous studies [19], which emphasize the importance of selecting appropriate VED values to efficiently guide the SLM process and rapidly identify suitable laser processing parameters for high-entropy alloy powders.

3.1.2. *Microstructure*

Fig. 4 shows the micromorphology and elemental distribution on the side of the specimen. In Fig. 4a, multiple melt pools are outlined by white dashed lines, each containing a mixture of grain types, including both equiaxed and columnar. This complex microstructure results from the unique thermal conditions present during the SLM process. As depicted in Figs. 4b and 4c, the rapid solidification rate characteristic of SLM generates significant thermal stresses, which in turn promotes the epitaxial growth of columnar dendrites extending from the melt pool boundary toward its center. In Fig. 4d, the result shows the coexistence of columnar crystals and isometric crystals. However, as the thermal gradient decreases toward the center of the melt pool, the driving force for directional growth diminishes, leading to the formation of equiaxed crystals in these regions. Furthermore, Fig. 4e highlights columnar dendrites exhibiting a variety of growth directions. This variation arises from the changing laser scanning direction employed during the layer-by-layer printing process. By periodically altering the scanning direction, thermal stress accumulation is reduced, and the local temperature gradient is modified, resulting in diverse dendrite orientations within the microstructure.

An excessively rapid cooling rate during the SLM process further influences the microstructure by promoting the formation of finer sub-grains. This is primarily due to the steep thermal gradients and the complex interactions that occur between the solidified material and the newly deposited layers. As a result, isometric, cell-like structures develop within the alloy at laser power of 320 W and laser speed of 400 mm/s, as illustrated in Fig. 4 f. These refined microstructural

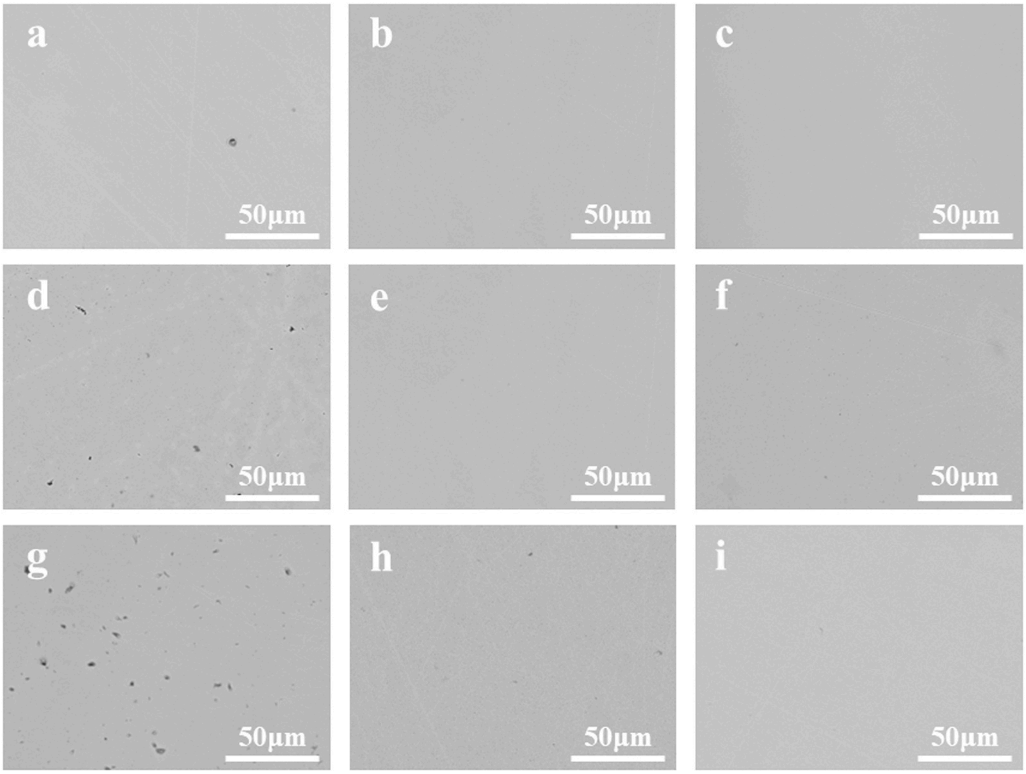

Fig. 3. Effect of laser parameters on porosity of different high-entropy alloy specimens prepared by SLM: (a) 200 W, 400 mm/s; (b) 200 W, 800 mm/s; (c) 200 W, 1200 mm/s; (d) 320 W, 400 mm/s; (e) 320 W, 800 mm/s; (f) 320 W, 1200 mm/s; (g) 440 W, 400 mm/s; (h) 440 W, 800 mm/s; (i) 440 W, 1200 mm/s.

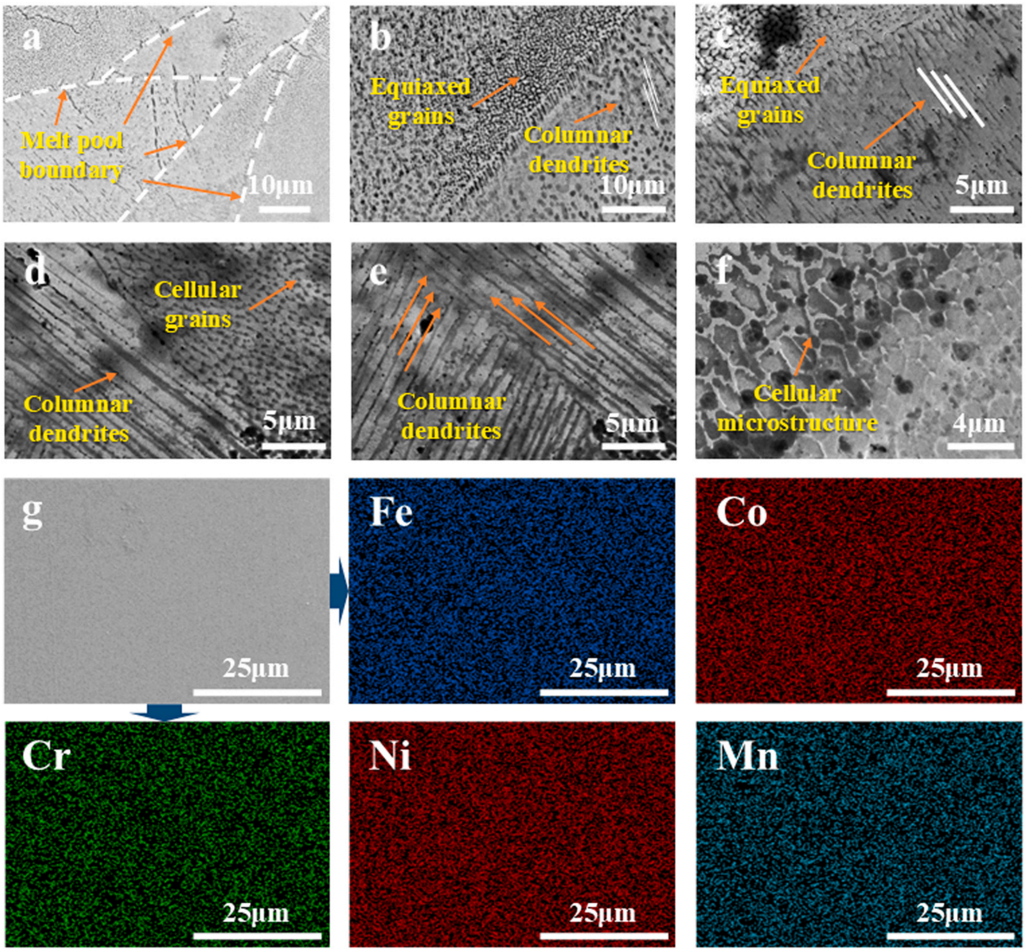

Fig. 4. (a)-(c) SEM images of high-entropy alloy with 200 W and 1200 mm/s; (d)-(f) SEM images of high-entropy alloy with 320 W and 400 mm/s; (g) EDS results: of different high-entropy alloy specimens prepared by SLM with 200 W and 400 mm/s.

features have a significant impact on the mechanical behavior of FeCoCrNiMn specimens produced via laser printing. The material contains numerous fine dendritic substructures with varying orientations, which interlace and entangle throughout the matrix. Additionally, the presence of fine, honeycomb-like grain boundaries enhances the ability of the material to store dislocations and absorb deformation energy. This hierarchical arrangement, comprising melt pools, dendritic columnar grains, and cellular grains, contributes to a notable improvement in mechanical properties, such as strength and toughness. These observations are consistent with previous studies [20], which have reported similar hierarchical microstructures in SLM-fabricated high-entropy alloys. Furthermore, Fig. 4 g displays the elemental distribution on the specimen surface, revealing that Fe, Co, Cr, Ni, and Mn are uniformly distributed without any evidence of segregation or aggregation. This uniform elemental distribution can be attributed to the rapid cooling rates inherent to the SLM process, which effectively suppress the tendency for elemental segregation during solidification.

In fact, the morphology of crystals is highly sensitive to laser parameters, particularly regarding crystal growth orientation and size variations. This sensitivity leads to anisotropic mechanical properties in the material. For instance, due to increased grain boundaries, columnar grains growing along the laser-molding direction typically exhibit high strength and high ductility perpendicular to their growth axis. Typically, smaller crystals contain more grain boundaries, making fine grain size a key factor influencing material mechanical properties. These crystal variations are all closely related to laser parameters.

3.1.3. Grain morphology

The inverse pole figures provide detailed information about the grain structure and orientation as influenced by the VED during laser processing. At lower volumetric energy densities (Figs. 5a–5c), the microstructure is characterized by the clear presence of laser trajectory lines on the specimen surface. Along these lines, fine grains are formed and tend to align with the direction of the laser scan, resulting in a tessellated, mosaic-like grain structure. This occurs because the lower energy input leads to rapid cooling and solidification, which limits grain growth and encourages the formation of small, regularly arranged grains. As the VED increases, the microstructure undergoes significant changes. The grains become noticeably larger, and the overall crystal morphology becomes less regular and more disordered, as shown in Figs. 5g–5i. This change is primarily due to the slower cooling rates associated with higher energy input, which allows grains more time to grow. Additionally, the dynamics of the melt pool become more complex, and intergranular anisotropy becomes more pronounced. These factors together promote the growth of grains in multiple directions, leading to a more irregular and less uniform grain structure.

The evolution of grain orientation with increasing energy density is also evident in the inverse pole figures. At low volumetric energy densities (Figs. 5a–5c), the (001) orientation is dominant, as indicated by the large red regions in the figures. This suggests that grain growth is strongly influenced by the thermal gradient, resulting in epitaxial growth along the build direction. However, as energy density increases, the dominance of the (001) orientation diminishes. Instead, other orientations such as (111) and (101) become more prevalent, which is reflected by the appearance of blue and green regions in the inverse pole

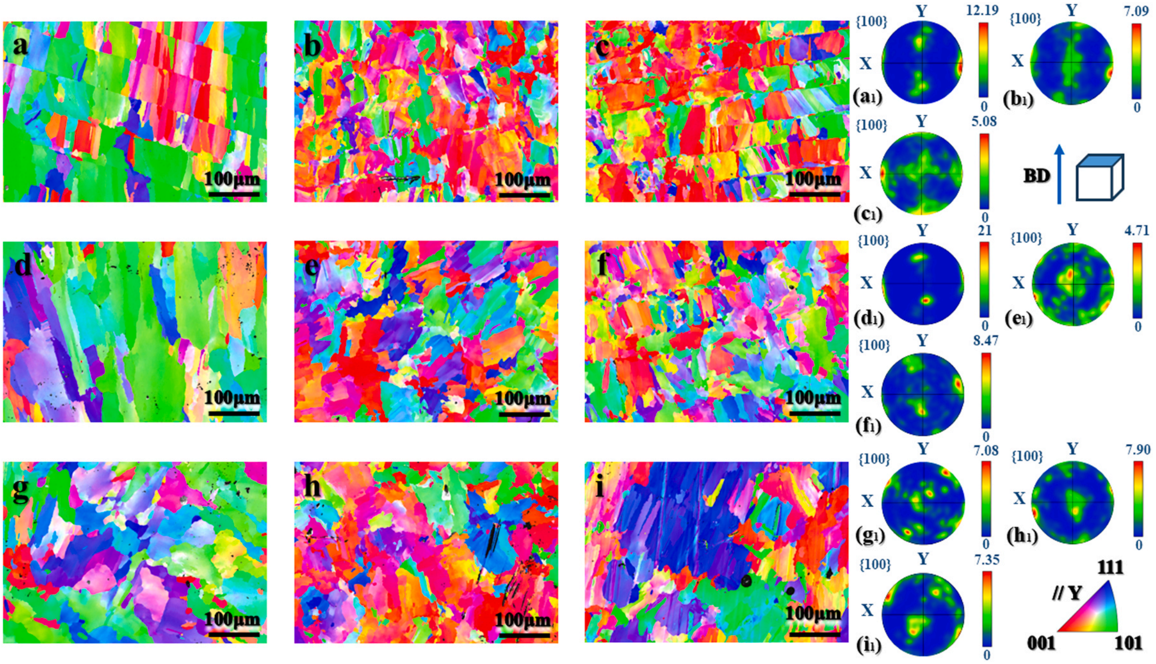

Fig. 5. IPF of X-Y plane on FeCoCrNiMn samples by SLM: (a) 200 W, 400 mm/s; (b) 200 W, 800 mm/s; (c) 200 W, 1200 mm/s; (d) 320 W, 400 mm/s; (e) 320 W, 800 mm/s; (f) 320 W, 1200 mm/s; (g) 440 W, 400 mm/s; (h) 440 W, 800 mm/s; (i) 440 W, 1200 mm/s, and PF of X-Y plane on FeCoCrNiMn sample by SLM: (a_1) 200 W, 400 mm/s; (b_1) 200 W, 800 mm/s; (c_1) 200 W, 1200 mm/s; (d_1) 320 W, 400 mm/s; (e_1) 320 W, 800 mm/s; (f_1) 320 W, 1200 mm/s; (g_1) 440 W, 400 mm/s; (h_1) 440 W, 800 mm/s; (i_1) 440 W, 1200 mm/s.

figures (Figs. 5d–5i). This shift indicates that the grains are growing in a wider variety of directions, reducing the overall texture strength. Pole figure analysis further supports these observations. For example, when the laser power is set to 320 W and the scanning speed to 400 mm/s, the maximum texture strength reaches a value of 21. Such a high texture strength means that a significant number of grains are aligned in a preferred crystallographic direction, which can enhance mechanical properties along those directions.

Fig. 6 shows the histograms of particle size distribution for the printed specimens under various processing conditions. Although some larger, inhomogeneous particles are present, the overall trend indicates that the average grain size increases as the VED rises. For example, when the laser power is set to 200 W and the printing speed is 1200 mm/s, as shown in Fig. 6c, the average grain size is relatively small, measuring 9.37 µm. In contrast, under higher energy input conditions, specifically, a laser power of 440 W and a printing speed of 400 mm/s, as shown in Fig. 6 g, the average grain size increases significantly to 23.32 µm. This increase in grain size with higher VED can be attributed to changes in the thermal environment during the printing process. At lower energy densities, the material cools and solidifies rapidly, which restricts grain growth and results in finer grains. Conversely, higher energy densities lead to slower cooling rates, allowing grains more time to grow and coarsen, thus producing a coarser microstructure. The variation in grain size has important implications for the mechanical properties of the printed specimens. According to the classical Hall–Petch relationship, there is an inverse correlation between grain size and material strength: as grain size decreases, the strength of the material typically increases because the higher density of grain boundaries impedes dislocation motion. Furthermore, grain refinement can enhance the formation of deformation twins, which also contributes to strengthening the material. The influence of grain size on the density and distribution of grain boundaries, as well as the role of deformation twins, are critical factors that should be further investigated in future analyses to fully understand their impact on the mechanical behavior of the printed specimens.

3.2. *Tensile properties and fractured behavior*

3.2.1. *Tensile properties*

Fig. 7a–c displays the engineering stress–strain curves for FeCoCrNiMn specimens produced using different combinations of laser power and scanning speed. When the laser power is set to 200 W and the scanning speed is 1200 mm/s, the specimens achieve a tensile strength of 634.45 MPa. The maximum engineering strain is observed at a laser power of 320 W and a scanning speed of 800 mm/s, indicating optimal ductility under these conditions.

Fig. 7d–f presents the true stress–strain curves. In Fig. 7d, it can be seen that, at a constant laser power of 200 W, increasing the scanning speed leads to a slight reduction in both tensile strength and ductility. This suggests that higher scanning speeds at lower laser power may not provide sufficient energy for optimal microstructural development, resulting in weaker and less ductile specimens. When the laser power is increased to 320 W, both tensile strength and ductility initially improve as the scanning speed increases, reaching their highest values at 800 mm/s. This indicates that there is an optimal combination of laser power and scanning speed that promotes favorable microstructural characteristics, such as balanced grain size and reduced porosity, which enhance mechanical performance. However, if the scanning speed is increased further beyond this point, both strength and ductility begin to decline, likely due to insufficient energy input for complete melting and bonding. At the highest laser power of 440 W, the influence of scanning speed on tensile properties persists, but the overall mechanical performance of the specimens deteriorates. This decline is primarily attributed to the excessive VED, which can lead to increased porosity and the formation of defects within the material. Such defects compromise both strength and ductility, underscoring the importance of optimizing processing parameters to achieve good mechanical properties.

Table 2 presents the yield strength, ultimate tensile strength, and average tensile ratio for each set of printing parameters. The results indicate that samples with a VED below 277.78 J/mm^3 generally exhibit higher tensile strength and elongation than those processed at VED value above this threshold. Among samples printed at VED value below

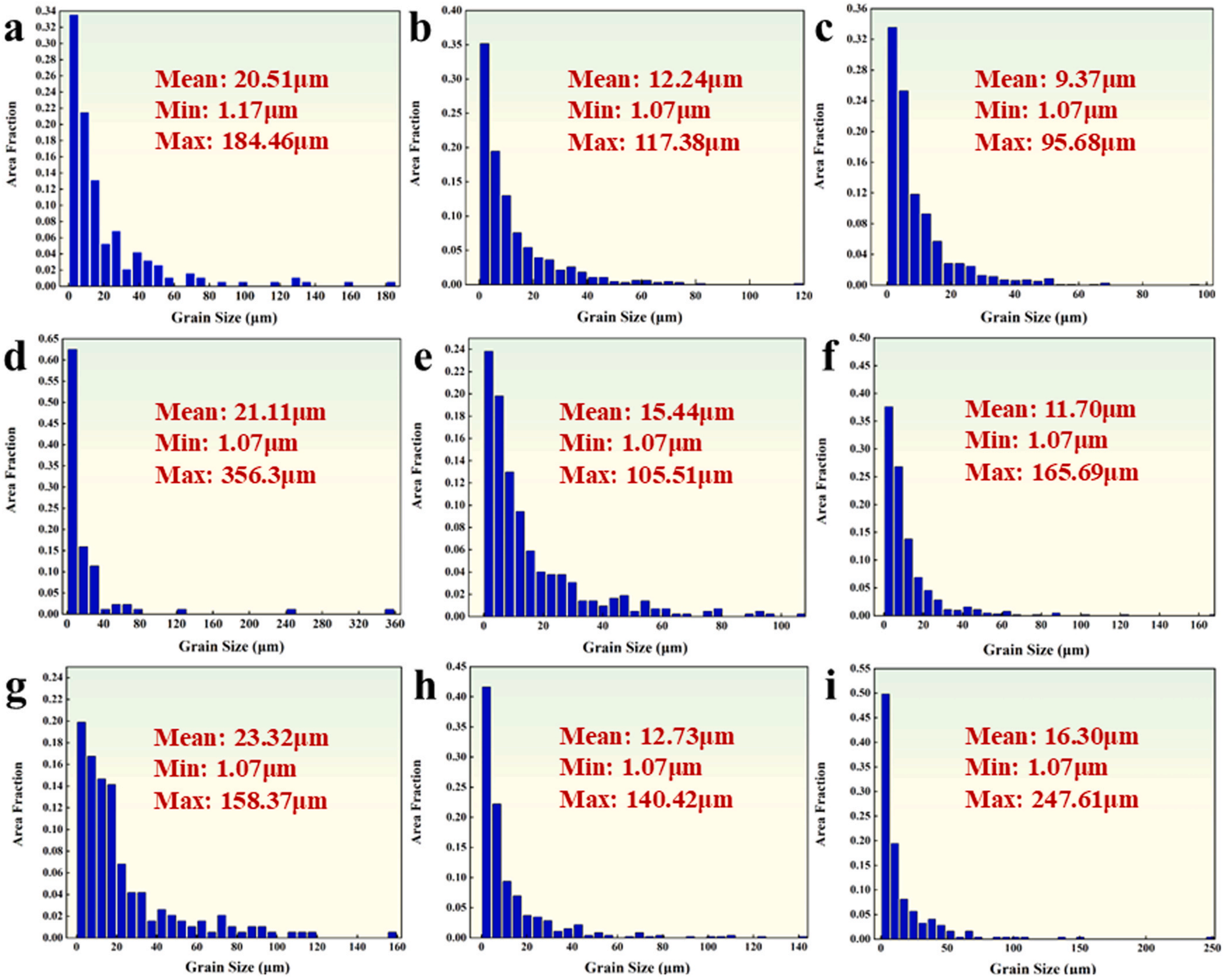

Fig. 6. Grain size distribution of FeCoCrNiMn samples by SLM: (a) 200 W, 400 mm/s; (b) 200 W, 800 mm/s; (c) 200 W, 1200 mm/s; (d) 320 W, 400 mm/s; (e) 320 W, 800 mm/s; (f) 320 W, 1200 mm/s; (g) 440 W, 400 mm/s; (h) 440 W, 800 mm/s; (i) 440 W, 1200 mm/s.

277.78 J/mm^3 , lower VED is associated with higher tensile strength, whereas higher VED correspond to greater elongation. These findings are consistent with the trends discussed earlier. According to the Hall–Petch relationship [21,22], smaller grains increase the number of grain boundaries, which impede dislocation motion and enhance strength. According to the results presented in Table 2, Fig. 3, and Fig. 6, samples printed at VED below 277.78 J/mm^3 generally exhibit reduced porosity. Under these processing conditions, the sample fabricated with a laser power of 200 W and a scanning speed of 1200 mm/s exhibited high tensile strength, attributed to its fine grain size of 9.37 μm. The highest yield strength (YS) and ultimate tensile strength (UTS) reached 547.72 MPa and 634.45 MPa, respectively. For the sample processed at a VED of 277.78 J/mm^3 , the grain size increased to 20.51 μm, resulting in a reduced tensile strength of 493.16 MPa. Additionally, the highest uniform tensile elongation (UTE) of 29.381 % is observed at 320 W and 800 mm/s. As shown in Fig. 5, most grain orientations align with BD//(100) due to the high thermal gradients and residual stresses that promote columnar grain growth along the build direction. The maximum texture strength of 21, observed at 320 W and 800 mm/s, indicates that many grains grew parallel to this direction. Ji et al. [23] reported that a higher density of columnar grains perpendicular to the direction of strain enhances the material's ability to store deformation energy, which explains the high tensile ratio observed under these conditions. For samples with VED exceeding 277.78 J/mm^3 , increased VED elevates both porosity and crystal grain size, leading to a simultaneous decrease in tensile strength and elongation. Furthermore, the rapid solidification inherent to SLM contributes to the formation of a tessellated grain structure. This complex microstructure enhances tensile performance, as shown in Fig. 5, and highlights the importance of carefully controlling laser parameters to achieve optimal mechanical properties.

Fig. 8 shows the work hardening rate of different specimens. The strain hardening rate at the beginning of stretching is higher for laser power of 200 W and 440 W, but it shows a slow increasing trend as the curve decreases, where the specimen with laser power of 200 W and laser printing speed of 1200 mm/s shows a higher work hardening rate. When the laser power is 320 W and the laser printing speed is 800 mm/s, the strain hardening curve first decreases and then increases and maintains a stable trend. According to the related research [24,25], these phenomena are mainly related to the formation of twins and dislocation entanglements. As the strain continues to increase, twins begin to form and gradually increase, and the twins will combine with various forms of dislocations, and even dislocation entanglement, so the interaction between these defects usually leads to higher strain hardening rate. It should be mentioned that the curves of these specimens all belong to the same type, with the curves first decreasing in a steep trend, then increasing slightly, and finally decreasing slowly. This indicates

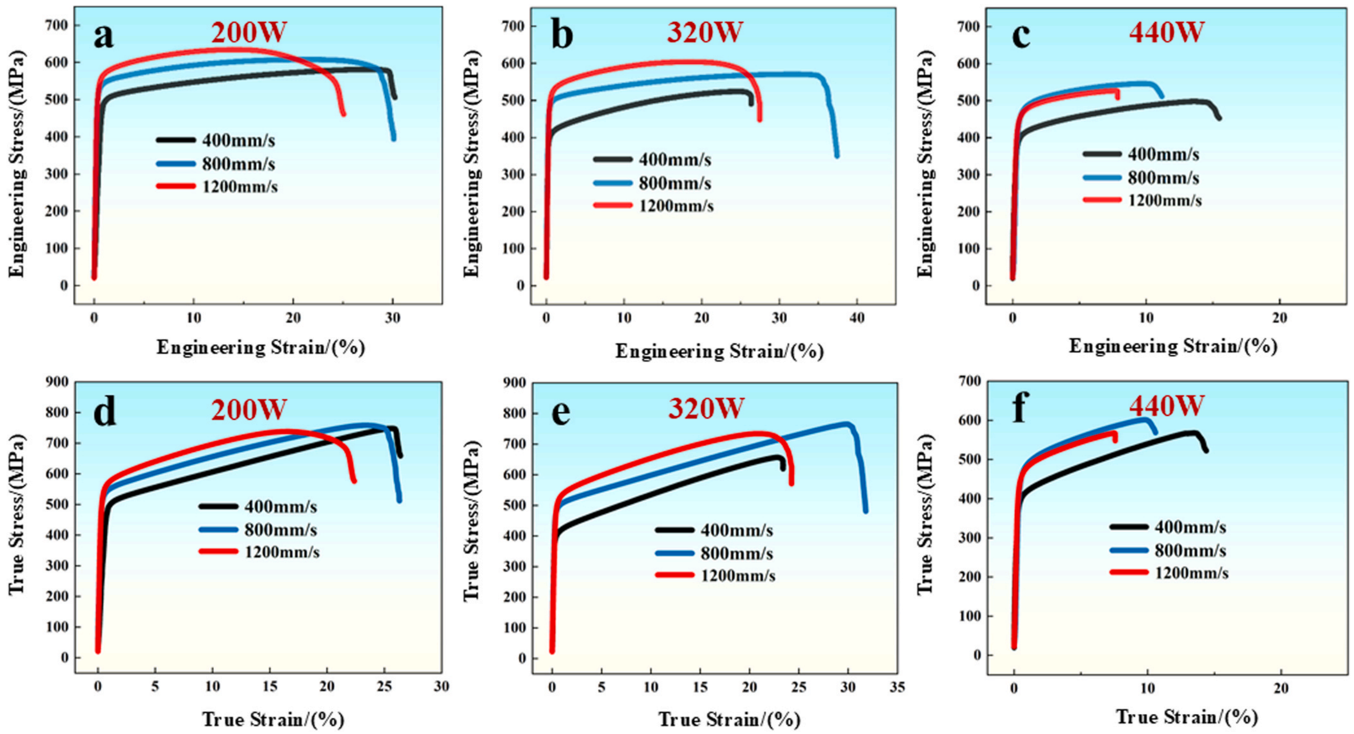

Fig. 7. Tensile properties of FeCoCrNiMn samples by SLM: (a-c) engineering stress and strain; (d-f) true stress and stain.

Table 2
Tensile characteristics of FeCoCrNiMn samples deposited by SLM with different laser parameters.

High-entropy alloy	Laser power (W)	Scanning velocity (mm/s)	VED (J/mm^3)	YS (MPa)	UTS (MPa)	UTE (%)
FeCoCrNiMn	200	1200	92.59	547.72 ± 19	634.45 ± 23	17.332 ± 4
	200	800	138.89	530.33 ± 26	607.67 ± 33	23.483 ± 6
	200	400	277.78	493.16 ± 9	581.27 ± 28	25.125 ± 2
	320	1200	148.15	511.81 ± 11	604.20 ± 16	21.025 ± 3
	320	800	222.22	489.53 ± 38	570.78 ± 10	29.381 ± 5
	320	400	444.44	399.17 ± 14	524.10 ± 18	22.672 ± 4
	440	1200	203.70	458.37 ± 20	526.72 ± 24	6.996 ± 1
	440	800	305.56	453.75 ± 6	546.20 ± 15	9.437 ± 2
	440	400	611.11	401.72 ± 24	498.32 ± 7	13.165 ± 3

that the FeCoCrNiMn specimens printed using the selective laser printing technique have a similar strain hardening tendency.

Fig. 9 provides a visual representation of the different stages involved in the evolution of work-hardening behavior, as previously depicted in Fig. 8. In Fig. 9a, the specimen is shown in its initial, undeformed state before any tensile stress is applied. At this stage, the crystal structure remains intact and unaltered. As tensile loading is applied, the specimen begins to deform. The crystal lattice elongates along the direction of the applied force, which corresponds to the initial stage in Fig. 8 where the work-hardening rate drops sharply. This rapid decrease in work-hardening rate is typically associated with the early stages of plastic deformation, where dislocation movement is relatively easy due to the low density of obstacles within the crystal. With continued loading, the deformation process becomes more complex. Dislocations, line defects within the crystal lattice, begin to multiply and interact. Additionally, deformation twins, which are mirror-image regions within the crystal structure, start to form. The accumulation and interaction of these defects increase the resistance to further deformation, causing the work-hardening rate to transition from a rapid decline to a more gradual increase [26], as observed in the subsequent stage of the curve in Fig. 8. This stage reflects the material's ability to sustain further plastic deformation while simultaneously increasing its strength.

3.2.2. *Fracture behavior*

To further investigate the effects of microstructure and crystal morphology on tensile properties, the fractured specimens were analyzed using electron backscatter diffraction (EBSD). As shown in Fig. 10g–i, when the laser power is 440 W, the high bulk energy density results in increased porosity, with numerous voids and cracks appearing on the specimen surface after tensile testing. The crystal morphology becomes disordered, indicating poor tensile performance. In contrast, at a laser power of 220 W, specimens fabricated at different scanning speeds exhibit preferential grain orientation along the (001)//BD and (111)//BD directions, with grains elongated along the tensile axis after uniaxial stretching. Numerous deformation twins and dislocation slip bands are observed in Fig. 10a–f, particularly in the specimen printed at 320 W and 800 mm/s. The distinctive tessellated structures formed by SLM are also visible in Fig. 10b–c. These nearly square checkerboard-like structures, composed of larger grains surrounded by finer crystals, undergo deformation during tensile loading. This microstructural configuration enhances stability under uniaxial tension and facilitates dislocation storage, thereby increasing tensile strength. Consequently, specimens fabricated at 200 W exhibit higher yield and tensile strengths, as shown in Table 2.

These findings further confirm that grain refinement and increased grain boundary density significantly enhance tensile properties, especially when using selective laser melting. However, at 320 W, the elevated VED leads to a steep thermal gradient in the melt pool, causing the checkerboard structure to diminish and larger columnar grains to

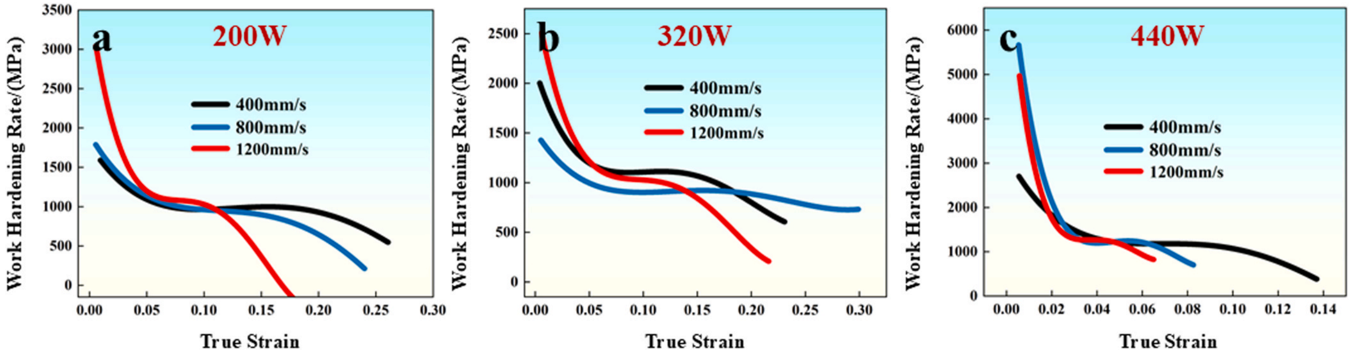

Fig. 8. Working hardening rate of FeCoCrNiMn samples by SLM.

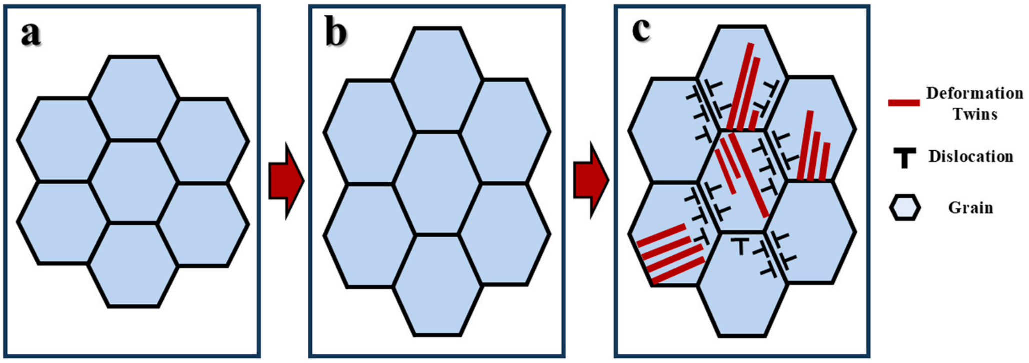

Fig. 9. Schematic diagram of working hardening rate evolution of FeCoCrNiMn samples by SLM.

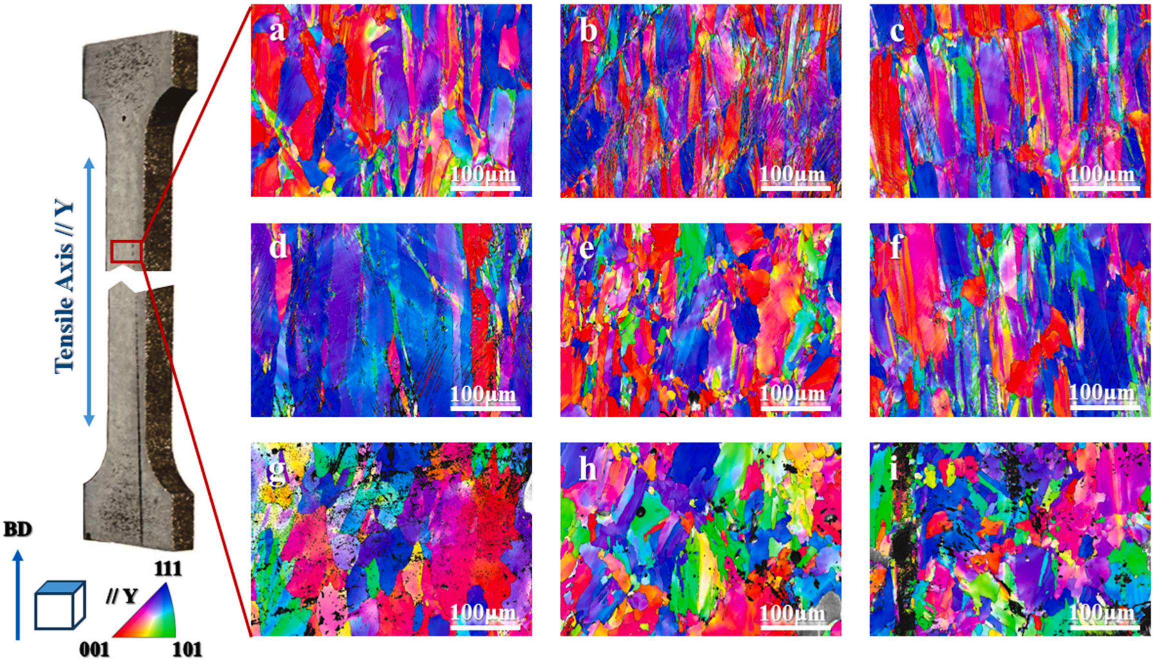

Fig. 10. IPF of X-Y plane on FeCoCrNiMn samples by SLM after tensile test: (a) 200 W, 400 mm/s; (b) 200 W, 800 mm/s; (c) 200 W, 1200 mm/s; (d) 320 W, 400 mm/s; (e) 320 W, 800 mm/s; (f) 320 W, 1200 mm/s; (g) 440 W, 400 mm/s; (h) 440 W, 800 mm/s; (i) 440 W, 1200 mm/s.

form. As a result, tensile strength decreases, while elongation increases due to the anisotropic mechanical behavior of columnar grains. As shown in Fig. 10d, these grains exhibit a (111) fiber texture along the tensile direction, with numerous slip bands—indicative of dislocation slip. According to the research of Bai et al. [27], coarse grains can accommodate larger dislocations due to their size and orientation, which enhances plastic deformation capacity.

The deformation strengthening mechanism of laser-printed FeCoCrNiMn high-entropy alloys primarily arises from increased twin formation and the impediment of dislocation motion by grain

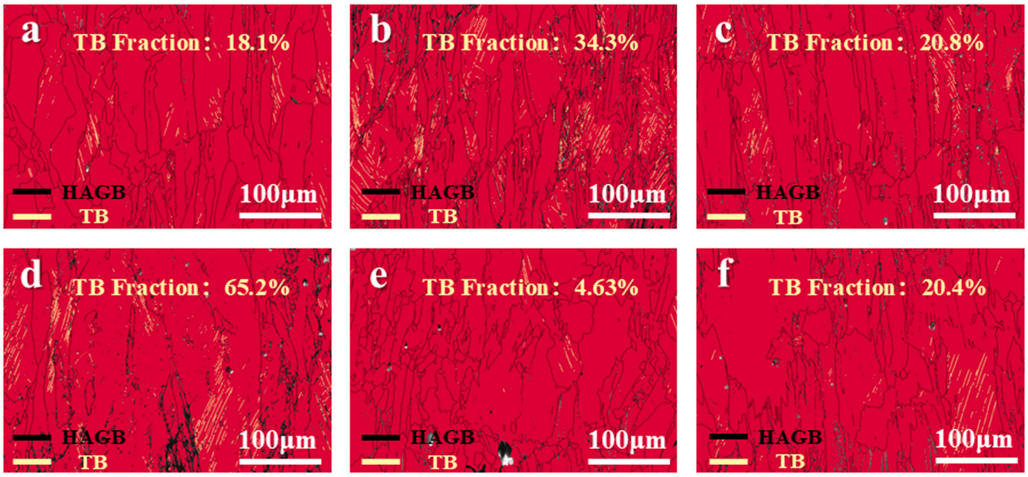

Fig. 11. Phase map with slip cracks and deformation twins of FeCoCrNiMn samples by SLM after tensile test: (a) 200 W, 400 mm/s; (b) 200 W, 800 mm/s; (c) 200 W, 1200 mm/s; (d) 320 W, 400 mm/s; (e) 320 W, 800 mm/s; (f) 320 W, 1200 mm/s.

boundaries. Fig. 11 illustrates the presence of deformation twins and dislocation slip in various tensile specimens. Notably, a high density of twins and dislocation activity is observed in the specimens fabricated at 220 W with a printing speed of 800 mm/s and at 320 W with a printing speed of 400 mm/s, which may be related to crystal orientation and grain boundary number. The corresponding twinning ratios for these specimens are 34.3 % and 65.2 %, respectively. These observations are consistent with the tensile performance trends shown in Fig. 7 and Table 2. Numerous studies have demonstrated [28–30] that twins, due to their unique crystallographic characteristics, can interact with dislocations in multiple ways. On one hand, an increased density of twins can effectively hinder dislocation motion, thereby enhancing strain

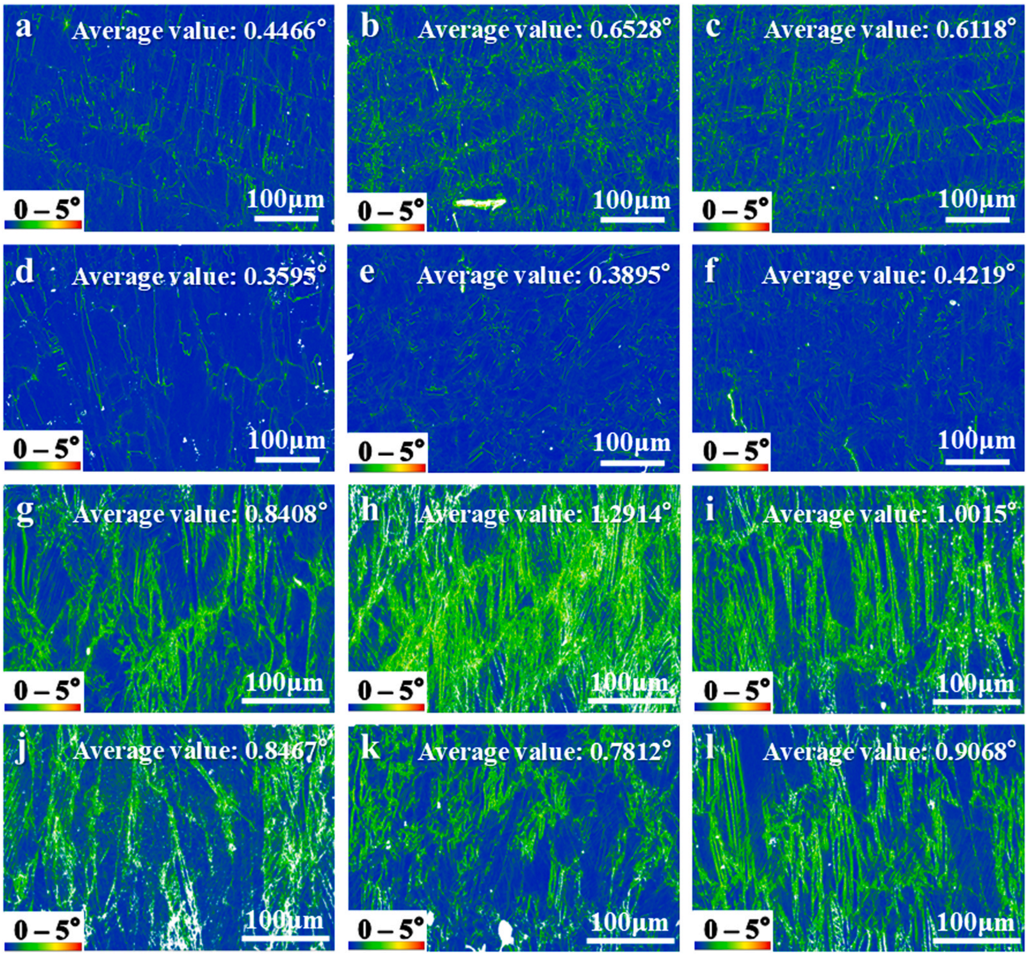

Fig. 12. KAM image of FeCoCrNiMn samples by SLM before tensile test: (a) 200 W, 400 mm/s; (b) 200 W, 800 mm/s; (c) 200 W, 1200 mm/s; (d) 320 W, 400 mm/s; (e) 320 W, 800 mm/s; (f) 320 W, 1200 mm/s; and after tensile test:: (g) 200 W, 400 mm/s; (h) 200 W, 800 mm/s; (i) 200 W, 1200 mm/s; (j) 320 W, 400 mm/s; (k) 320 W, 800 mm/s; (l) 320 W, 1200 mm/s.

hardening. On the other hand, twins can also serve as additional slip planes, accommodating more dislocations and contributing to the material's plastic deformation capacity.

The kernel average orientation (KAM) is used to evaluate residual stress distribution in materials and can reveal both thermal residual stresses prior to deformation and tensile-induced residual stresses after stretching. Fig. 12 illustrates the KAM maps of various specimens. By comparing Figs. 12a–c and 12d–f, it is evident that specimens fabricated at lower volumetric energy densities exhibit higher KAM values, with residual stresses primarily concentrated along the boundaries of the laser melt pools. This is attributed to the rapid cooling rates and severe thermal gradients inherent to the SLM process. As shown in Fig. 12g–l, KAM values increase significantly after tensile testing, with higher values observed at grain boundaries compared to grain interiors. In specimens produced with lower energy densities (e.g., Fig. 12 h), elevated KAM values are concentrated at tessellated microstructural junctions and within fine grains, indicating that residual stresses are absorbed at grain boundaries. These stresses are associated with high dislocation densities and stacking faults, indirectly reflecting increased dislocation accumulation. In contrast, specimens fabricated at higher energy densities (e.g., Fig. 12j) show elevated KAM values within coarse columnar grains, suggesting that dislocation accumulation occurs predominantly through intragranular mechanisms. Coarse grains accommodate larger dislocations and exhibit enhanced plastic deformability, while fine grains, due to their higher grain boundary density, store more dislocations and contribute to increased tensile strength.

In conclusion, the enhancement of tensile properties and strain hardening behavior in these alloys is closely linked to dislocation accumulation and twinning induced by grain refinement. The comparative analysis of KAM distributions further supports the conclusions drawn from earlier mechanical and microstructural evaluations.

Fig. 13 illustrates the fracture morphology of tensile specimens fabricated under different laser parameters. As shown in Fig. 13–f, specimens produced with higher bulk energy densities exhibit a greater number of internal voids. This is primarily due to the formation of gas pores during the laser melting of metal powders. Elevated volumetric energy densities can lead to unstable melt pools and the formation of keyholes—deep, narrow cavities that are difficult to fill during solidification—ultimately compromising the mechanical integrity of the printed parts. Fig. 14 provides a magnified view of the fracture surfaces from selected specimens in Fig. 13. Despite the presence of numerous pores and cracks, dimpled structures characteristic of ductile fracture are also observed. These local ductile dimples coexist with these holes and cracks. This indicates that fractured behavior is not purely brittle but rather a combination of brittle and ductile mechanisms. Generally, specimens with fewer pores and cracks exhibit more ductile dimple structures and a higher proportion of ductile fracture. Moreover, the presence of microporous structures in some prints may contribute positively to fracture toughness by promoting energy absorption during crack propagation.

However, further research is needed to understand and control the interaction between microporous structures and the surrounding microstructure. Such insights are essential for optimizing laser printing parameters to fabricate high-performance metallic components with complex geometries and enhanced mechanical properties.

3.3. Microhardness and wear

To comprehensively evaluate the properties of the high-entropy alloy specimens fabricated via selective laser melting, both microhardness and wear resistance were systematically assessed. Fig. 15 presents the microhardness values of specimens produced under different laser parameters. The results indicate that microhardness is higher at lower laser powers and decreases with increasing laser power, suggesting that the microhardness of the specimens is related to changes in porosity, with higher microhardness observed at lower porosities. For instance, under low bulk energy density conditions—such as a laser power of 200 W and a scanning speed of 400 mm/s—the microhardness reaches a maximum of 267 HV. In contrast, at a higher bulk energy density (440 W, 400 mm/s), the microhardness drops to 219 HV. The indentation images in Fig. 15 further demonstrate that bulk energy density significantly influences specimen densification, which in turn affects hardness. Specimens produced at higher energy densities exhibit more cracks and pores around the indentation sites, indicating reduced structural integrity and lower

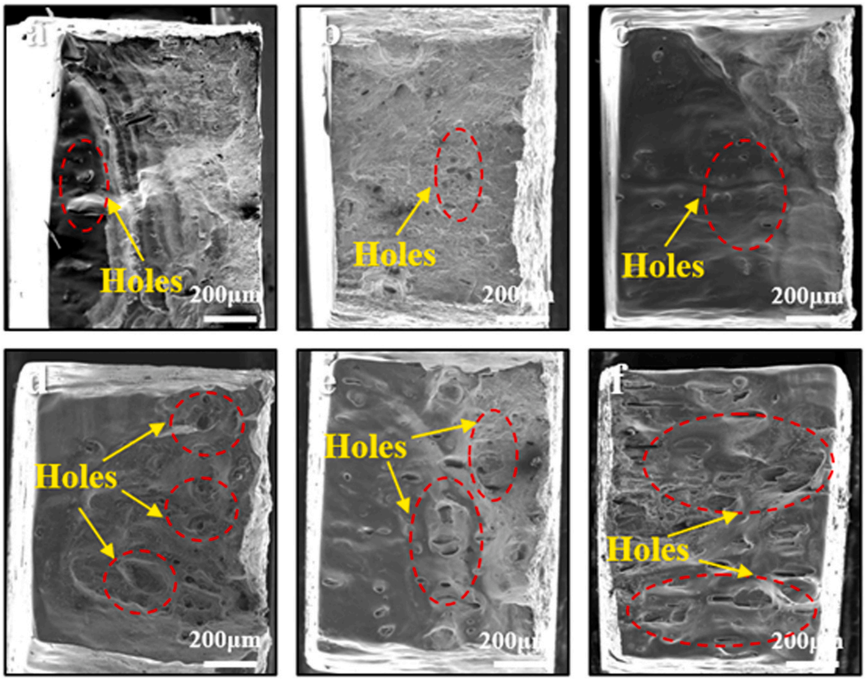

Fig. 13. The fracture micromorphology of FeCoCrNiMn samples by SLM after tensile test: (a) 200 W, 400 mm/s; (b) 200 W, 800 mm/s; (c) 200 W, 1200 mm/s; (d) 320 W, 400 mm/s; (e) 320 W, 800 mm/s; (f) 320 W, 1200 mm/s.

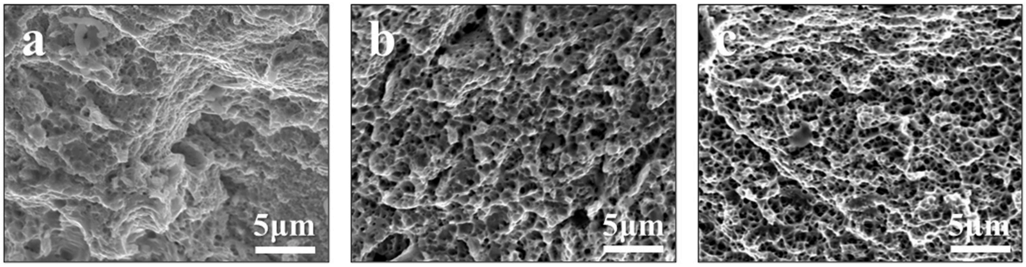

Fig. 14. The magnified fracture micromorphology of FeCoCrNiMn samples by SLM after tensile test: (a) 200 W, 800 mm/s (138.89 J/mm3); (b) 320 W, 800 mm/s (222.22 J/mm3); (c) 200 W, 400 mm/s (227.78 J/mm3).

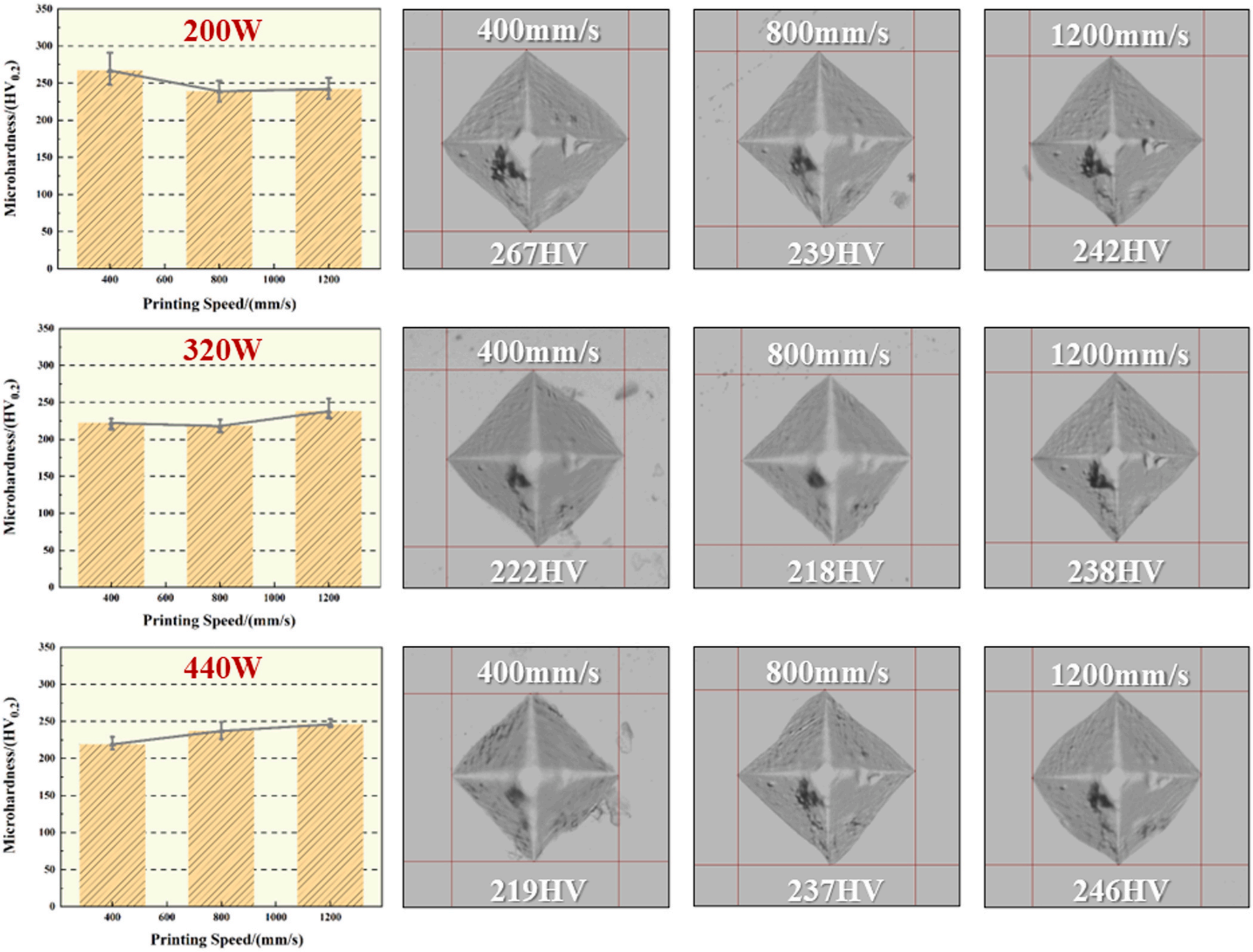

Fig. 15. Microhardness of FeCoCrNiMn samples by SLM.

resistance to localized deformation.

Fig. 16 presents the coefficient of friction for specimens fabricated under different laser parameters. The friction coefficient curves for all specimens exhibit a gradual increase followed by stabilization. This behavior is attributed to the initial stage of testing, during which the grinding balls are not yet in full contact with the specimen surface, resulting in a lower friction coefficient. As contact improves, the coefficient increases and eventually reaches a steady state. Since hardness significantly influences wear performance, the friction coefficient trends closely mirror the hardness variations observed in the specimens. At a laser power of 200 W, the friction coefficients across different scanning speeds are generally higher than those observed at 320 W and 440 W. Additionally, the friction curves at 200 W show smaller fluctuations, indicating more stable wear behavior. This variation is also influenced by internal crystal morphology and dislocation resistance. As shown in Figs. 6 and 10, an increase in fine grains leads to a higher grain boundary density, which, along with increased dislocation density, enhances wear resistance. The elevated and more fluctuating friction coefficient observed in Fig. 16 g may be due to the presence of micropores formed under high VED. These microstructural features disrupt surface uniformity and contribute to increased variability in frictional behavior.

Subsequently, the wear rates of the specimens were calculated and compared, as shown in Fig. 17. When the laser power was 200 W, the wear rates of specimens at different printing speeds remained below

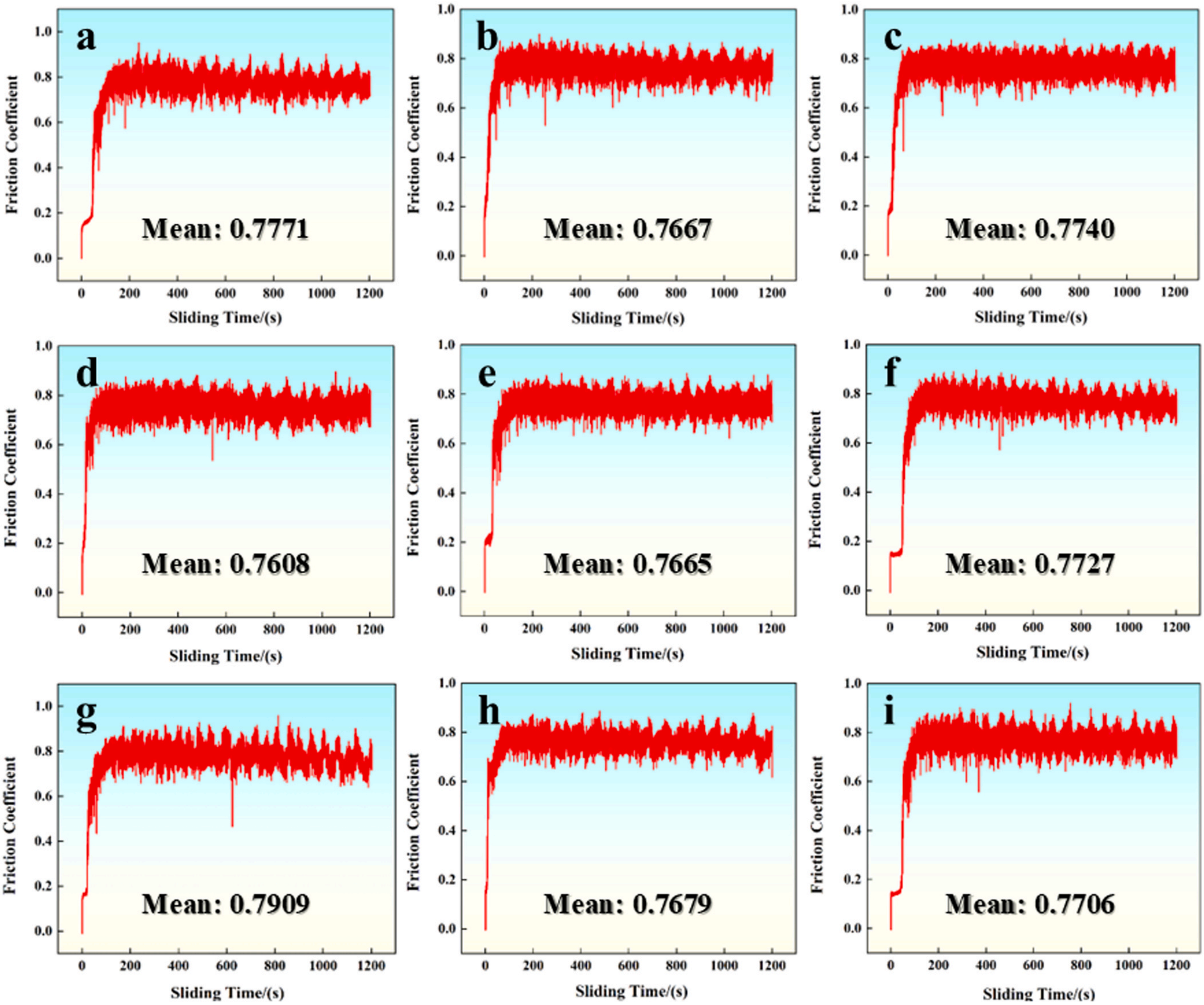

Fig. 16. Friction coefficient of FeCoCrNiMn samples by SLM: (a) 200 W, 400 mm/s; (b) 200 W, 800 mm/s; (c) 200 W, 1200 mm/s; (d) 320 W, 400 mm/s; (e) 320 W, 800 mm/s; (f) 320 W, 1200 mm/s; (g) 440 W, 400 mm/s; (h) 440 W, 800 mm/s; (i) 440 W, 1200 mm/s.

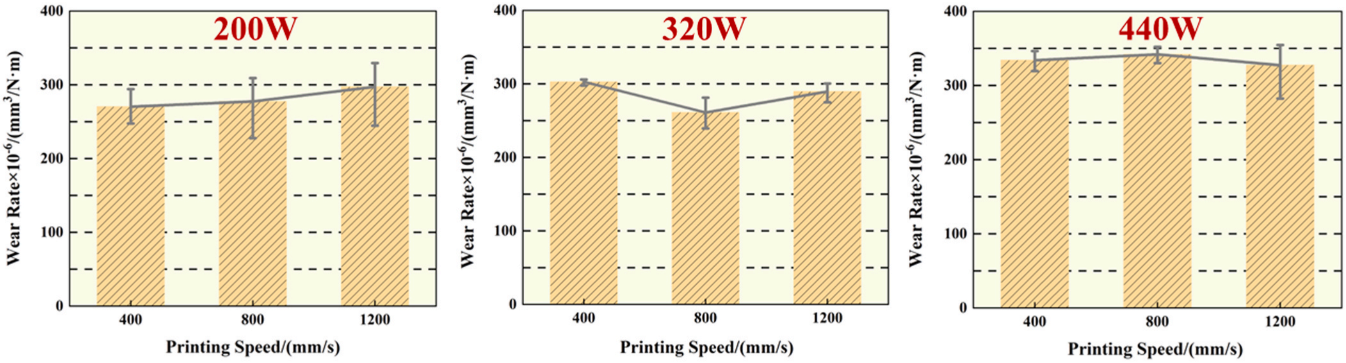

Fig. 17. Wear rate of FeCoCrNiMn samples by SLM.

300 mm^3 /N·m. Observations of wear morphology in Fig. 18 further revealed that specimens with superior wear resistance—such as those printed at 200 W and 400 mm/s—exhibited shallow wear grooves, with depths as low as 55.62 μm. These findings suggest that mechanical properties such as tensile strength, microhardness, and wear resistance exhibit similar trends across varying laser parameters. Hardness plays a critical role in determining wear performance. Generally, higher hardness correlates with increased friction coefficients and reduced wear rates. This relationship holds true for specimens fabricated at laser powers of 220 W and 320 W, were increasing printing speed leads to

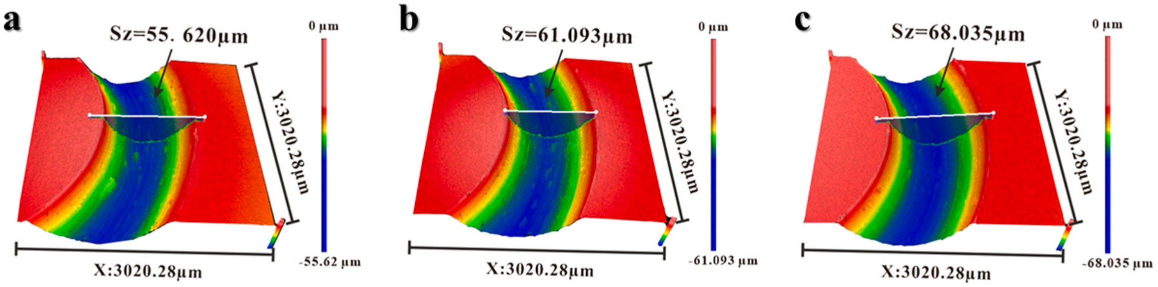

Fig. 18. Surface morphology of the wear tracks for FeCoCrNiMn samples by SLM: (a) 200 W, 400 mm/s; (b) 320 W, 400 mm/s; (c) 440 W, 400 mm/s.

higher hardness and correspondingly higher friction coefficients. However, specimens produced at 440 W display more variability in wear performance. Some of these samples exhibit hardness values exceeding 230 HV and relatively high friction coefficients yet still demonstrate substantial wear rates. This phenomenon is primarily attributed to the enhanced ductility and toughness of the material. According to the research of Du et al. [31], during friction and wear testing, surface hardening occurs under normal stress as material is removed. Materials with greater ductility and toughness exhibit higher surface hardening rates, allowing them to better resist wear and material loss. Conversely, specimens with lower ductility and toughness require less energy for crack initiation and propagation, resulting in higher wear rates.

4. Conclusions

This research involved the impact of varying laser power and laser speed on the microstructure and crystal morphology of FeCoCrNiMn high-entropy alloy prepared using the SLM technique. The mechanical properties of the specimens are further analyzed based on these structures and morphologies. The study yielded the following specific findings:

1) The increase in VED may lead to instability in the melt pool and the formation of numerous pores, thereby increasing the specimen's porosity. When the VED is below 277 J/mm^3 , the sample exhibits reduced surface porosity and improved surface smoothness. In contrast, when the VED exceeds 611.11 J/mm^3 , the sample shows increased surface porosity and deteriorated surface smoothness. Due to the rapid solidification rate of SLM technology, the FeCoCrNiMn specimen exhibits a microstructure characterized by the coexistence of melt pool traces, columnar crystals, and equiaxed crystals, featuring uniform elemental distribution without segregation.
2) A lower VED results in finer grains and a checkerboard-like crystal structure, and the crystal orientation is typically aligned along the (001) direction. The maximum texture strength can reach 21, which contributes to enhanced mechanical properties of the sample perpendicular to the growth direction. In contrast, a higher VED promotes crystal growth, weakens the (001) orientation, enhances the (111) and (101) orientations, and leads to a more irregular and complex crystal morphology.
3) SLM-printed FeCoCrNiMn specimens exhibit excellent tensile properties perpendicular to the build direction, primarily due to the preferential growth of most crystals along the temperature gradient. Laser volume energy density influences grain size, with finer grains increasing the number of grain boundaries and generating more twins during deformation, which in turn enhances the yield strength and ultimate tensile strength of the specimen. Coarse-grained structures, due to their larger size, can accommodate more dislocations and promote twin formation, but also result in a fracture mode dominated by intragranular fracture, accompanied by a higher uniform elongation rate. Among samples with volumetric energy densities below 277.78 J/mm^3 , the volumetric energy density was 92.59 J/mm^3 with a maximum tensile strength of 547.72 MPa. When the volumetric energy density reached 222.22 J/mm^3 , the maximum elongation at break was 29.381 %.
4) The microhardness of the specimen is correlated with its porosity, and it gradually decreases as the laser energy density increases. Samples with higher hardness typically exhibit good wear resistance, and toughness and ductility exert a more significant influence on wear resistance. Samples with good toughness require higher energy to initiate cracks, thus resisting material removal. When the laser power is set to 200 W and the printing speed is 400 mm/s, the samples exhibit lower wear rate and wear depth.

CRediT authorship contribution statement

Muhammad Rehan: Methodology, Investigation, Formal analysis, Data curation. **Jiani Huang:** Visualization, Validation, Software, Methodology, Investigation. **Tao He:** Writing – original draft, Validation, Methodology, Investigation, Formal analysis, Data curation, Conceptualization. **Wai Sze Yip:** Writing – original draft, Visualization, Supervision, Resources, Methodology, Funding acquisition, Formal analysis, Data curation. **Yinhui Wang:** Supervision, Software, Resources, Methodology. **Juan Chen:** Visualization, Validation, Methodology, Investigation. **Wenjie Lu:** Writing – review & editing, Supervision, Methodology, Investigation. **Linhe Sun:** Validation, Methodology, Investigation, Formal analysis. **Suet To:** Validation, Software, Investigation, Funding acquisition, Formal analysis, Data curation. **Hui Deng:** Validation, Supervision, Methodology, Investigation. **Xusheng Yang:** Visualization, Validation, Supervision, Formal analysis.

Declaration of Competing Interest

The authors declare that they have no known competing financial interests or personal relationships that could have appeared to influence the work reported in this paper.

Acknowledgements

The authors acknowledge the financial supports from Young Scientist Fund of National Natural Science Foundation of China (Project No.: 52205498/K-ZGFT); the State Key Laboratory in Hong Kong from the Innovation and Technology Commission (ITC) of the Government of the Hong Kong Special Administrative Region (HKSAR), China; the General Research Fund (GRF) of the Research Grants Council (RGC) of the Hong Kong Special Administrative Region (HKSAR), China (Project No.: PolyU 15220724); and the Research Committee of The Hong Kong Polytechnic University (Project code: RMAC).

References

[1] Y.M. Wang, T. Voisin, J.T. McKeown, et al., Additively manufactured hierarchical stainless steels with high strength and ductility[J], Nat. Mater. 17 (1) (2018) 63–71.

[2] Z.G. Zhu, Q.B. Nguyen, F.L. Ng, et al., Hierarchical microstructure and strengthening mechanisms of a CoCrFeNiMn high entropy alloy additively manufactured by selective laser melting[J], Scr. Mater. 154 (2018) 20–24.
[3] Z. Tong, H. Liu, J. Jiao, et al., Microstructure, microhardness and residual stress of laser additive manufactured CoCrFeMnNi high-entropy alloy subjected to laser shock peening[J], J. Mater. Process. Technol. 285 (2020) 116806.
[4] W. Deng, S. Xing, M. Chen, Effect of annealing treatments on microstructure, tensile and wear properties of cold-rolled FeCoCrNiMn high entropy alloy[J], J. Mater. Res. Technol. 27 (2023) 3849–3859.
[5] S. Chen, Y. Tong, P.K. Liaw, Additive manufacturing of high-entropy alloys: a review[J], Entropy 20 (12) (2018) 937.
[6] A. Fu, Z. Xie, J. Wang, et al., Controlling of cellular substructure and its effect on mechanical properties of FeCoCrNiMo0, 2 high entropy alloy fabricated selective laser melting[J]. Materials Science Engineering A 901 (2024) 146547.
[7] J. Wang, H. Yang, Z. Liu, et al., Compositional regulation in additive manufacturing of precipitation-hardening (CoCrNi) 94Ti3Al3 medium-entropy superalloy: Cellular structure stabilization and strength enhancement[J], Composites Part B Engineering 281 (2024) 111570.
[8] F. Otto, A. Dlouhý, C. Somsen, et al., The influences of temperature and microstructure on the tensile properties of a CoCrFeMnNi high-entropy alloy[J], Acta Mater. 61 (15) (2013) 5743–5755.
[9] B. Cantor, I.T.H. Chang, P. Knight, et al., Microstructural development in equiatomic multicomponent alloys[J], Materials Science Engineering A 375 (2004) 213–218.
[10] Z. Zhou, K. He, Q. Liu, et al., Effects of LPBF printing parameters on the columnar-to-equiaxed grain transition in FeCoCrNiMn alloys[J], Sci. Rep. 15 (1) (2025) 21893.
[11] J. Zhang, Y. Yan, B. Li, Selective Laser Melting (SLM) additively manufactured CoCrFeNiMn high-entropy alloy: process optimization, microscale mechanical mechanism, and high-cycle fatigue behavior[J], Materials 15 (23) (2022) 8560.
[12] Z. Xu, H. Zhang, W. Li, et al., Microstructure and nanoindentation creep behavior of CoCrFeMnNi high-entropy alloy fabricated by selective laser melting[J], Addit. Manuf. 28 (2019) 766–771.
[13] S. Liu, M. Hu, L. Xiao, et al., Effects of strain rate and low temperature on dynamic behaviors of additively manufactured CoCrFeMnNi high-entropy alloys[J], Materials Science Engineering A 913 (2024) 147100.
[14] Y. Chew, G.J. Bi, Z.G. Zhu, et al., Microstructure and enhanced strength of laser aided additive manufactured CoCrFeNiMn high entropy alloy[J], Materials Science Engineering A 744 (2019) 137–144.
[15] R. Li, P. Niu, T. Yuan, et al., Selective laser melting of an equiatomic CoCrFeMnNi high-entropy alloy: Processability, non-equilibrium microstructure and mechanical property[J], J. Alloy. Compd. 746 (2018) 125–134.
[16] M. Zheng, C. Li, X. Zhang, et al., The influence of columnar to equiaxed transition on deformation behavior of FeCoCrNiMn high entropy alloy fabricated by laser-based directed energy deposition[J], Addit. Manuf. 37 (2021) 101660.
[17] Y. Li, Z. Zhang, Q. Wu, et al., Enhanced corrosion resistance of FeCoCrNiMn high-entropy alloy in aqueous H2SO4 solutions by N and Si alloying[J], J. Mater. Eng. Perform. (2025) 1–12.
[18] D. Gu, Y.C. Hagedorn, W. Meiners, et al., Densification behavior, microstructure evolution, and wear performance of selective laser melting processed commercially pure titanium[J], Acta Mater. 60 (9) (2012) 3849–3860.
[19] B. Li, L. Zhang, Y. Xu, et al., Selective laser melting of CoCrFeNiMn high entropy alloy powder modified with nano-TiN particles for additive manufacturing and strength enhancement: Process, particle behavior and effects[J], Powder Technol. 360 (2020) 509–521.
[20] L. Guo, J. Gu, B. Gan, et al., Effects of elemental segregation and scanning strategy on the mechanical properties and hot cracking of a selective laser melted FeCoCrNiMn-(N, Si) high entropy alloy[J], J. Alloy. Compd. 865 (2021) 158892.
[21] C. Zhang, K. Feng, H. Kokawa, et al., Cracking mechanism and mechanical properties of selective laser melted CoCrFeMnNi high entropy alloy using different scanning strategies[J], Materials Science Engineering A 789 (2020) 139672.
[22] J.Y. He, H. Wang, H.L. Huang, et al., A precipitation-hardened high-entropy alloy with outstanding tensile properties[J], Acta Mater. 102 (2016) 187–196.
[23] P. Ji, Y. Jia, P. Ma, et al., Exceptional strength–ductility combination of CoCrFeMnNi high-entropy alloy with fully recrystallized structure by selective laser melting after post-deformation annealing[J], J. Mater. Res. Technol. 23 (2023) 3166–3176.
[24] H. Cheng, H. Luo, Z. Pan, et al., Effects of laser powder bed fusion process parameters on microstructure and hydrogen embrittlement of high-entropy alloy [J], J. Mater. Sci. Technol. 155 (2023) 211–226.
[25] S. Liu, M. Hu, L. Xiao, et al., Effects of strain rate and low temperature on dynamic behaviors of additively manufactured CoCrFeMnNi high-entropy alloys[J], Materials Science Engineering A 913 (2024) 147100.
[26] S. Yang, Y. Liu, H. Chen, et al., Laser powder bed fusion of Fe60 (CoCrNiMn) 40 medium-entropy alloy with excellent strength-ductility balance[J], Mater. Des. 238 (2024) 112720.
[27] Y. Bai, H. Jiang, K. Yan, et al., Phase transition and heterogeneous strengthening mechanism in CoCrFeNiMn high-entropy alloy fabricated by laser-engineered net shaping via annealing at intermediate-temperature[J], J. Mater. Sci. Technol. 92 (2021) 129–137.
[28] A.G. Wang, X.H. An, J. Gu, et al., Effect of grain size on fatigue cracking at twin boundaries in a CoCrFeMnNi high-entropy alloy[J], J. Mater. Sci. Technol. 39 (2020) 1–6.
[29] S.J. Sun, Y.Z. Tian, X.H. An, et al., Ultrahigh cryogenic strength and exceptional ductility in ultrafine-grained CoCrFeMnNi high-entropy alloy with fully recrystallized structure[J]. Materials Today, Nano 4 (2018) 46–53.
[30] H. Wang, D. Chen, X. An, et al., Deformation-induced crystalline-to-amorphous phase transformation in a CrMnFeCoNi high-entropy alloy[J], Sci. Adv. 7 (14) (2021) eabe3105.
[31] J. Du, J. Huang, C. Tan, et al., Effect of thermal history control on mechanical properties of laser powder bed fusion maraging steel[J], Mater. Charact. 224 (2025) 115049.